American Mineralogist, Volume 110, pages 1886–1897, 2025

Using multimodal X-ray computed tomography to advance 3D petrography: A non-destructive investigation of olivine inside a carbonaceous chondrite

Matthew J. Pankhurst[1,2,*,†], Jette Oddershede[3], Rhian H. Jones[4], Daniel M. Thorley[4], Olivia A. Barbee[3,5], Nghia T. Vo[6], Katherine J. Dobson[7], Andrew Bodey[8], and David Eastwood[9,10]

[1]Environmental Research Division, Instituto Tecnológico y de Energías Renovables (ITER), 38611, Granadilla de Abona, Tenerife, Canary Islands, Spain
[2]Gaiaxiom Pty Ltd, Vasbygade 10A, 2450 Copenhagen, Denmark
[3]Xnovo Technology ApS, Galoche Allé 15, 1. 4600 Køge, Denmark
[4]Department of Earth and Environmental Sciences, The University of Manchester, Manchester M13 9PL, U.K.
[5]Geology Department, Whitman College, 345 Boyer Avenue, Walla Walla, Washington 99362, U.S.A.
[6]Brookhaven National Laboratory, National Synchrotron Light Source II, Building 741, Room 140, P.O. Box 5000, Upton, New York 11973-5000, U.S.A.
[7]Department of Civil and Environmental Engineering, University of Strathclyde, James Weir Building, 75 Montrose Street, Glasgow G11 XJJ, U.K.
[8]Diamond Light Source Ltd, Harwell Science & Innovation Campus, Oxfordshire OX11 0DE, U.K.
[9]The University of Manchester at Harwell, Diamond Light Source, Harwell Campus, Didcot, Oxfordshire OX11 0DE, U.K.
[10]Department of Mechanical and Aerospace Engineering, The University of Manchester, Manchester, M13 9PL, U.K.

Abstract

Rocks form in three dimensions through time and studying them provides information from inside dynamic systems we cannot otherwise observe. Yet how we typically access the interior of the rocks themselves to gain that information may limit our understanding and influence how we reconstruct the processes that formed them. Here, we demonstrate combined non-destructive 3D X-ray imaging techniques that produce quantitative densitometric and crystallographic maps of entire individual grains inside a rock. Olivine grains throughout a sample of the carbonaceous chondrite Northwest Africa (NWA) 11346 were each characterized by size, shape, composition, zoning intensity, and crystallographic orientation. The addition of 3D crystallographic mapping to calibrated 3D densitometric analysis—used to calculate chemical composition—demonstrates a fully non-destructive petrographic method and provides unique insight. For instance, in our case, using crystallographic data to delineate individual grains and then measuring the 3D size, shape, and composition of each distinguishes variably reset relict grains from those later crystallized after a melting event. Intersection in a 2D slice could not have led to this interpretation because the integration of three-dimensional size, rounding, composition, location, and crystallographic orientation measured from each grain forms the key patterns. Multimodal laboratory X-ray imaging has strong potential to advance 3D petrography.

Keywords: Three-dimensional petrography, chondrite, olivine, crystallographic orientation, LabDCT, X-ray tomography, non-destructive

Introduction

Since thin-section petrography was developed in the mid-19th century and continues today, dissecting rocks to access their interiors is requisite to the majority of techniques used to analyze their texture, chemistry, mineralogy, and age. Although causing irrevocable loss of context (Carlson and Denison 1992), two-dimensional petrography has provided foundational understanding. The relatively few studies that gain full 3D access to rocks demonstrate that there can be more to learn if destructive access to the information within is avoided or at least delayed until later in an integrated analytical workflow. This is because rock records are multi-dimensional, over time recording conditions and dynamics in their mineral structures and compositions, crystallographic orientations and twinning, sizes, shapes, imperfections, and inclusions, which all have a physical 3D context. Destructive analysis precludes out-of-plane observations of the size and shape of individual grains as well as their spatial relationships, also meaning that integration of chemical data cannot be firmly linked to physical size, shape, or location. Hence, conventional access to a rock limits access to the full multidimensional physicochemical record it contains. The numerous approaches developed to tackle how we should use 2D observations to solve 4D puzzles, such as ionic diffusion chronometry to investigate magmatic timescales and crystal size distributions to investigate nucleation and growth rates, attest to this (Marsh 1998; Morgan and Jerram 2006; Kahl et al. 2011; Pankhurst et al. 2018b; Cashman 2020; Ostorero et al. 2022).

Non-destructive petrography

X-ray micro-computed tomography (micro-CT) imaging produces 3D images of density contrast and was pioneered at brilliant (high-flux) light sources at synchrotron radiation facilities (see

* Corresponding author E-mail: mjp@gaiaxiom-geoscience.com Orcid https://orcid.org/0000-0001-6844-9822

0003-004X/25/0012–1886$05.00/DOI: https://doi.org/10.2138/am-2023-9213

Jones 1999). The application of laboratory-based (low-flux) absorption contrast tomographic imaging commenced within the geosciences over 30 years ago (Carlson and Denison 1992) and has since grown in step with generational advances in power and stability of the X-ray sources, optical solutions to magnification, broadening data acquisition options, and a relative decrease in the cost of computational power over the past decades (see Cnudde and Boone 2013). Micro-CT affords volumetric analysis of individual grains (e.g., Kuebler et al. 1999), 3D relational observations (e.g., Philpotts et al. 1999), and a perspective that provides full representation of variability at small scales (e.g., Taylor et al. 2000). In cases where sufficient density contrast between and within grains exists, absorption micro-CT can address numerous petrographic questions (e.g., Mock and Jerram 2005; Jerram and Higgins 2007; Jerram et al. 2009; George and Gaidies 2017; Hanna and Ketcham 2017; Mourey and Shea 2019; Couperthwaite et al. 2021; Lubbers et al. 2023). In addition to 3D measurement and visualization, advantages include minimal and fast sample preparation (Pankhurst et al. 2014) and no requirement for vacuum or special environmental conditions.

Quantitative densitometry can be used to obtain chemical information from absorption contrast images, which requires either a monochromatic beam or knowledge of the energy distribution of a polychromatic beam (Uesugi et al. 2010; Pankhurst et al. 2018a, 2018c). However, even if the grayscale intensities of absorption images are quantitative and reproducible, because density itself is not diagnostic of mineralogy, a priori knowledge of the sample is essential for useful interpretations. The advent of laboratory diffraction contrast tomography (LabDCT) has the potential to advance 3D petrography by introducing an independent modality that is sensitive to crystallographic system and lattice parameters (McDonald et al. 2015; Holzner et al. 2016; Pankhurst et al. 2019).

Here, we have used 3D crystallographic measurements to distinguish crystals and delineate each from one another, even if they have similar density and are touching. Crystallographic information also allows for a novel visualization of each grain in a standardized orientation (i.e., orthorhombic axes are presented parallel to the x, y, z axes of a 3D image file). This treatment, when combined with quantitative absorption contrast images, enables petrographic analysis to become multi-dimensional and multi-contextualized, which we hypothesize can lead to novel insight.

Using olivine as a case mineral to advance 3D petrography

Olivine is a common rock-forming mineral in mafic and ultramafic igneous systems. It also occurs in some more evolved igneous systems, as well as in metamorphic and metasomatic assemblages. The petrography of olivine is a cornerstone of many important models, including mantle processes and mafic magmatism (e.g., Fleet 1978; Foley et al. 1987; Helz 1987; Fitton and Godard 2004; Hansen et al. 2012; Kin et al. 2017; Pankhurst et al. 2018b; Mourey and Shea 2019) and, more recently, carbon capture (e.g., Kerisit et al. 2013).

In this study, we investigate olivine in a carbonaceous chondritic meteorite (CM chondrite) as a record of solar system formation (e.g., Brearley and Jones 1998). Chondrules are igneous beads formed ~4.6 billion years ago in the protoplanetary disk during the melting of fine-grained precursor assemblages. The droplets then cooled at rates of tens to hundreds of degrees per hour, crystallizing olivine and pyroxene (Jones et al. 2017). There are two main types of chondrule: Type I chondrules, which are MgO-rich with typical olivine compositions $Fo_{95–100}$, and Type II chondrules, which are more FeO-rich, with olivine typically zoned in the range $Fo_{60–80}$ (Jones 2012). In the latter, individual olivine grains commonly have relict forsteritic cores ($Fo_{>90}$) derived from Type I chondrules. Olivine with grain sizes of tens to hundreds of micrometers occurs in chondrules and as isolated grains in CM chondrites.

Methods

Samples

Reference materials. Five olivine grains (two ~Fo_{75}, two ~Fo_{80}, and one at Fo_0) previously characterized by Pankhurst et al. (2018b) with backscattered electron (BSE) imaging and electron probe microanalysis (EPMA) were used as reference materials. They were selected to span a large range in Fo content, and the choice of grain "pairs" of very similar composition was made to test the precision of the subsequent calibration. The zoned grains have large (milimeter scale) homogeneous cores and comparatively narrow rims (~100 μm). Melt inclusions (and spinel inclusions) are few and clearly visible due to their highly contrasting densities, making them easy to avoid when measuring image intensity. The fayalite grain used, being appreciably denser than the others, was considerably smaller to enable suitable transmission of X-rays through all grains and allowed the five to be scanned together. No compositional zoning was encountered within the fayalite, which is distinct from coexisting phases that vein the fayalite (Rose et al. 2009) in both texture and density (see Pankhurst et al. 2018c). The grains were cut from their mounts using a hobby drill with a ~3 mm diameter coring bit prior to scanning. The little resin that surrounded those grains had no appreciable influence on X-ray attenuation or the results due to its much lower density. In all cases, image intensity data were obtained from compositionally homogenous, internal regions of olivine.

Carbonaceous chondrite, NWA 11346. Northwest Africa 11346 (NWA 11346) is a carbonaceous chondrite meteorite classified by Gattacceca et al. (2019) as CM-anomalous (CM-an). NWA 11346 is described as anomalous because it lacks phyllosilicates, which are typical of the aqueously altered CM (Mighei-like) group of carbonaceous chondrites. This observation points to the chondrite having been heated after aqueous alteration (King et al. 2021). For this study, a rectangular block of NWA 11346 measuring 0.8 × 2.5 × 5 mm was used for multimodal X-ray tomography. Its prismatic shape provided a contiguous volume of ~10 mm^3 that we anticipated would host numerous olivine grains, supporting a robust data set, while allowing tests of X-ray transmission through the short dimensions.

Analytical techniques

Near-monochromatic X-ray absorption contrast tomography (NM-ACT). X-ray absorption contrast tomography was conducted on the i13 beamline at the Diamond Light Source (U.K.). A heavily filtered pink beam produced a spectrum with a mean energy of 31 keV and a full-width half-maximum of 12 keV (Online Materials[1] Fig. S1). The five reference olivine grains were measured using a 120 ms exposure time and a single continuous helical scan. A helical scan was made of the NWA 11346 sample, together with one compositionally zoned terrestrial olivine grain also characterized by Pankhurst et al. (2018c) as an internal standard [see approach by Pankhurst et al. (2017)], under identical beam conditions during the same session, and the same style of Kapton tube holding the materials. The helical scan track was implemented for its advantages in suppressing ring artifacts (Pankhurst et al. 2018c; Vo et al. 2021) and for providing a single continual image of a long sample. The data processing pipeline included: flat-field correction, distortion correction (Vo et al. 2015), helical-circular conversion (Vo et al. 2021), rotation axis determination (Vo et al. 2014), partial ring-artifact removal (Vo et al. 2018), and filtered-back projection reconstruction (Ramachandran and Lakshminarayanan 1971). Voxel size was 1.125 μm (xyz) and data were saved as 32-bit tiff stacks. The height of the NWA 11346 sample that was scanned was limited in this experiment by the Z travel distance of the stage and the requirement

for reference crystals in the same scan. A chondrule exposed at the surface on one end was entirely captured (Online Materials[1] Fig. S2) and corresponds to the high-resolution LabDCT scan region of interest (ROI) (see below).

Calibration of forsterite concentration to NM-ACT image intensity. The raw image brightness values of the five pre-characterized olivine grains span most of the 32-bit range, an expected result due to selecting an appropriate exposure time so the projections could maximize raw image contrast. After tomographic reconstruction, central portions of the grains known to be compositionally homogeneous and free from remaining minor image artifacts were measured using standard image analysis tools in the open-source software FIJI (Schindelin et al. 2012). No image filtering was conducted as part of the calibration. The intensity values were plotted against the corresponding Fo values from Pankhurst et al. (2018c), and a linear fit was found. See Online Materials[1] Extended Methods for further background regarding the linear X-ray attenuation of the olivine group and approach to calibration. The same linear fit is found without using the fayalite sample and rules out this sample acting as an outlying lever upon the calibration. Scaling the intensity values to 8-bit (256 gray levels) was required for computation purposes. Yet, due to the considerable density difference between the fayalite and the other four Fo-rich grains, this down-scaling would render paired calibration grains indistinguishable from one another. Instead, a restricted range of the 32-bit image was selected to exclude the fayalite to better illustrate the contrast at the forsterite end of the solid solution. The 8-bit calibration was built using identical image regions and returned a linear fit with an R^2 value of 0.991 (see Table 1). A least squares regression was constructed by first considering the uncertainty on each EPMA result and image intensity value. Pankhurst et al. (2018c) reported an uncertainty of ±0.25 mol% for the EPMA data. Each average intensity value was obtained with a different number of contributing voxels (Table 1) and hence resulted in a different standard error of the mean for each data point. All image intensity standard deviations are comparatively much smaller than the EPMA uncertainty, leading to Mahalanobis distance, covariance, and chi-squared results supporting the choice of expressing uncertainty as a least squares regression and error envelope. First, the ±0.25 mol% uncertainty was added to the linear regression line. Within the range of the raw data, the Fo error was deemed to be ±0.25%. The maximum and minimum slopes constrained by this envelope were propagated outside the range, resulting in three error domains across the olivine solid solution (Fig. 1).

The same image intensity range was used to scale the NWA 11346 scan data from 32-bit to 8-bit, and hence arrive at a calibrated NM-ACT image of the contained olivine. The calibrated NM-ACT imaging provides sufficient accuracy and precision (and returns an R^2 of >0.99) for the purpose of olivine grain analysis, with the advantage of gathering volumetric compositional data using a non-destructive methodology.

Polychromatic absorption contrast tomography (P-ACT). P-ACT scans were conducted at Xnovo Technology ApS, Køge, Denmark, on a ZEISS Xradia 520 Versa X-ray Microscope equipped with a polychromatic, divergent X-ray source. The beam conditions used were 50 kV and 4 W with the low-energy LE3 filter to pre-harden the beam. Projections (n = 1601) of 5 s exposure time were collected around 360° rotation and reconstructed using a routine filtered back projection reconstruction algorithm supplied by ZEISS to reach a voxel size of 2.5 µm over a 2.5 mm tall portion of the sample cross section, without frame averaging. A P-ACT data set covering the entire sample was generated by consecutive scans using the same sample mount at different stage heights, then vertically stitching three such portions to record as a single 32-bit image (Fig. 2a).

Laboratory diffraction contrast tomography (LabDCT). The full P-ACT data set was coupled with a fast overview LabDCT scan—on the same Xradia 520 Versa microscope—of the whole sample to determine the positions and crystallographic orientations of individual olivine grains (Figs. 2b–2c). Based on these results, a 0.9 × 0.9 × 0.5 mm (hwd) region of interest (ROI) for a high-resolution P-ACT and LabDCT scan was located (a Type II chondrule: Figs. 2 and 3). Each

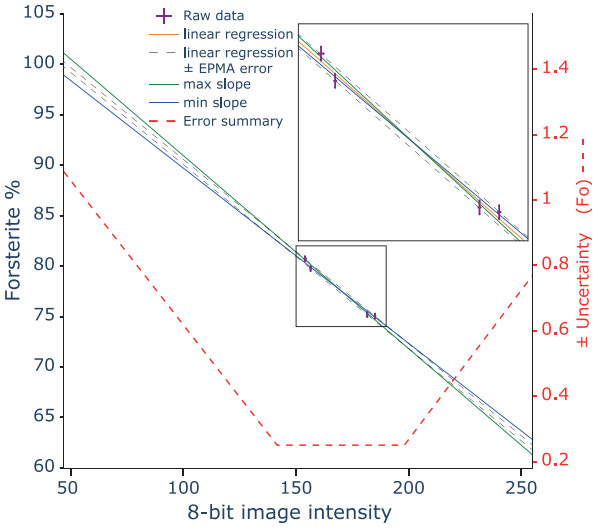

Figure 1. Calibration between olivine composition determined by EPMA and image intensity using a near-monochromatic X-ray beam. A linear relationship between X-ray attenuation coefficient and olivine composition is confirmed by the tight array. Least-squares regression and error propagation across the olivine solid solution utilize the precision of the EPMA within the range of raw data to form an uncertainty envelope, and the maximum and minimum slopes constrained by that envelope to estimate uncertainty outside the range of the raw data.

LabDCT scan was conducted immediately after the corresponding P-ACT scan without adjusting the sample on the rotation stage to ensure the best possible correlative imaging conditions.

LabDCT scans were conducted using the LabDCT Pro module at a source setting of 110 kV and 10 W after the insertion of both an aperture and a beamstop. Reconstruction of the LabDCT data was performed using the GrainMapper3D™ software (Bachmann et al. 2019), assuming lattice parameters corresponding to Fo_{80}. Experimenting with lattice parameters between $Fo_{0–100}$ produced no significant difference in the detection of grains.

The fast overview LabDCT scan of the entire sample was conducted with projection geometry using the Flat Panel detector and the Helical Phyllotaxis advanced acquisition scheme (Oddershede et al. 2022). 1079 projections of 6 × 10 s were collected using the 750 × 750 µm aperture, a source-to-sample distance of 30 mm, and a sample-to-detector distance of 245 mm. These settings were selected to cover a large sample volume for every projection, with the trade-off of the grain size detection limit being approximately 100 µm. Within the full sample, crystallographic orientations of 52 olivine grains larger than 100 µm were reconstructed. Regions of olivine were defined as belonging to the same grain if the misorientation between adjacent voxels (10 µm voxel size) was <5°, after which volume-weighted average grain orientations were computed.

The high-resolution LabDCT scan of the Type II chondrule (Fig. 4) was conducted as a conventional scan using the DCT4X detector in Laue focusing geometry. 201 projections of 300 s were collected using the 750 × 750 µm aperture, a source-to-sample distance of 12 mm, and a sample-to-detector distance of 11 mm. These settings were selected to be significantly more sensitive toward

Table 1. Olivine image brightness: Composition calibration data

Image analysis					EPMA	
Calibration grain	n voxels in area selection	Mean image intensity (8-bit)	Standard deviation of image intensity	Standard error of mean[a]	Fo (%)	Fo (%) uncertainty
G3	15456	185.01	30.72	±0.25	75.03	±0.25
G6	49772	181.59	40.54	±0.18	75.20	±0.25
G9	24532	156.44	28.37	±0.18	79.75	±0.25
G13	3176	153.99	26.22	±0.47	80.73	±0.25

[a] The standard deviation of the image intensity values of the selected area of a calibration grain is divided by the number of voxels within that area.

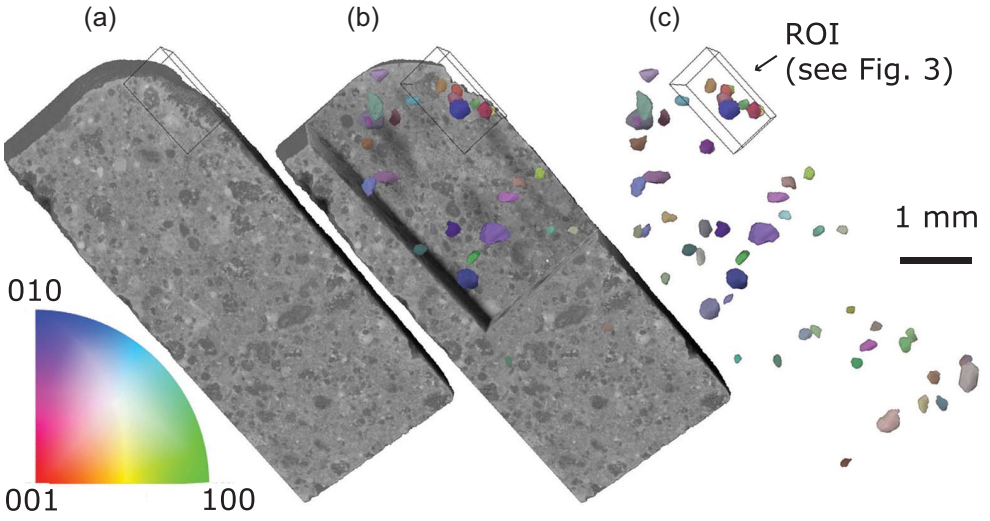

Figure 2. Results of P-ACT and LabDCT overview scans of NWA 11346 (carbonaceous chondrite). (**a**) P-ACT data maps density contrast within the sample, which highlights textural features such as mineral grains and matrix. (**b**) Partial P-ACT data cutaway of (**a**), highlighting the locations and shapes of olivine grains as reconstructed using diffraction contrast tomography. (**c**) Full cut-away revealing the spatial distribution and crystallographic orientation of every olivine grain >100 μm within the sample. The inverse pole figure color map is relative to the long axis of the sample. The outlined box indicates the location of the high-resolution LabDCT scan (see Fig. 4).

smaller grains in a limited sample volume. Within the ROI, crystallographic orientations of 77 olivine grains larger than 50 μm were reconstructed from the LabDCT data. Regions in space were defined as belonging to the same grain if the misorientation between adjacent voxels (2.5 μm voxel size) was <5°, after which volume-weighted average grain orientations were computed. The accuracy of the LabDCT technique can be assessed by the interfacial angles expected of olivine (see Fig. 4).

Post-X-ray imaging energy-dispersive spectroscopy. Scanning electron microscopy (SEM) techniques for in situ chemical and mineralogical analysis are typically more accessible than monochromatic beam imaging. To demonstrate a practical approach to link chemical composition with 3D observations, the sample was carefully, sequentially, ground and polished by hand using diamond paste to a 1 μm polish, which eventually exposed a surface that included the chondrule ROI selected for detailed study and several other chondrules. The heterogeneous and porous nature of the sample, as well as the fact that the chondrule ROI was on the edge of the block, made this a meticulous process. Knowledge of the 3D location and extent of the ROI chondrule prior to this step, together with the evidence of cracks, porosity, and hence fragility of the feature (see Fig. 3), guided the preparation and highlights the value of non-destructive in situ observation prior to any destructive technique. Quantitative analyses of individual olivine grains on the polished surface were obtained using energy-dispersive spectroscopy (EDS) on a FEI Quanta 650 field emission gun (FEG) SEM with a Bruker EDS detector, at the University of Manchester. Analyses were obtained at an accelerating voltage of 15 kV, a beam current of 2 nA, and X-ray counts for each analysis of 5 000 000. EDS analyses were quantified using the following standards: Mg on SW_olivine; Si on fayalite; Ca on wollastonite; Cr on chromite; Mn on tephroite. Estimated errors on Fo contents for EDS analyses are ±0.2 mol%.

Calibration and integration

Calibration of P-ACT data with NM-ACT and EDS. The integration of quantitative compositional data with crystallographic data first required calibration of the P-ACT image brightness to Fo values. This approach was taken because the co-location of P-ACT and LabDCT data is straightforward, owing to their measurement within the same instrument without movement of the sample. We also found that the P-ACT data has overall fewer image artifacts than the NM-ACT data and so were more useful when assessing fine textural features. Finally, due to the ease of co-location, grains are more accurately extracted and analyzed digitally in P-ACT rather than NM-ACT data. However, in contrast to the NM-ACT, the P-ACT data are not natively quantitative in terms of olivine composition and also may suffer from subtle beam hardening effects (see below).

A calibration was constructed by first measuring the grayscale intensity of corresponding regions in each data set and then taking the calculated Fo from calibrated NM-ACT data (see above) to assign to the grayscale intensity of the P-ACT data of the ROI. This secondary calibration returns Fo values of 100.0 and 99.7 for the cores of clearly relict grains and so demonstrates an accurate and fully non-destructive workflow. The linear relationship between P-ACT image brightness and Fo content is further verified by EDS (see below and Online Materials[1]).

Calculating compositional precision of the P-ACT data is not straightforward, however. Following Pankhurst et al. (2018c), we note that the use of P-ACT data to obtain compositional information on small scales near phase boundaries, such as crystal rims, should be approached with caution due to self-absorption of X-rays in the margins of a phase denser than its surroundings (beam hardening). These P-ACT data have not been beam-corrected, and hence the uncertainty on Fo composition values is likely to be dependent, in part, upon textural context. In broad homogeneous cores, the image noise typically converges on 1σ of ~250 (16-bit) brightness levels, which corresponds to ~1.25 Fo units. We therefore consider this to be a maximum precision in rim compositions.

Co-location of NM-ACT and Lab-DCT data is less trivial due to the different orientation of the sample during scanning. However, the integration of the composition and crystallography of a few grains was evaluated, selected based on their clear 3D habit and zonation, which allowed for confident verification. The calibrated NM-ACT data were rotated into the same orientation as the P-ACT data (as rotated to extract grains, see above) using Fijiyama (Fernandez and Moisy 2021), a plugin of FIJI. With all tomographic data oriented according to the crystallographic orientation of each grain, respectively, the NM-ACT data were also cropped to each of the selected grains (e.g., Fig. 4f). Detailed analysis of zonation profiles, including ionic interdiffusion chronology, is a separate study.

P-ACT data from the entire sample scan were compared with co-located EDS measurements of olivine from chondrules across the sample depth, including from the chondrule within the ROI. The Fo_{100} relict cores in the chondrule in the full-sample P-ACT scan are observed to be slightly brighter in back-scatter-electron images than Fo_{100} chondrules in the middle of the sample (see Online Materials[1]). This can be explained as an effect of subtle beam hardening, yet it does not influence our interpretation because our petrographic investigation is focused upon the chondrule and uses the NM-ACT for primary calibration and ROI P-ACT data for data integration and subsequent plotting and pattern recognition. The number and precision of the individual EDS measurements allow for a slightly tighter calibration across a wider Fo range to be built than that using the reference olivine and NM-ACT data (see Online Materials[1]), yet using either calibration makes no difference to the final interpretations.

Data integration to define individual grains. The LabDCT reconstruction produces 3D maps of the sample with individually labeled grains (represented by a single crystallographic domain and assigned a number), see Figure 3. The reconstructed LabDCT grains were combined with the high-resolution faceted grain

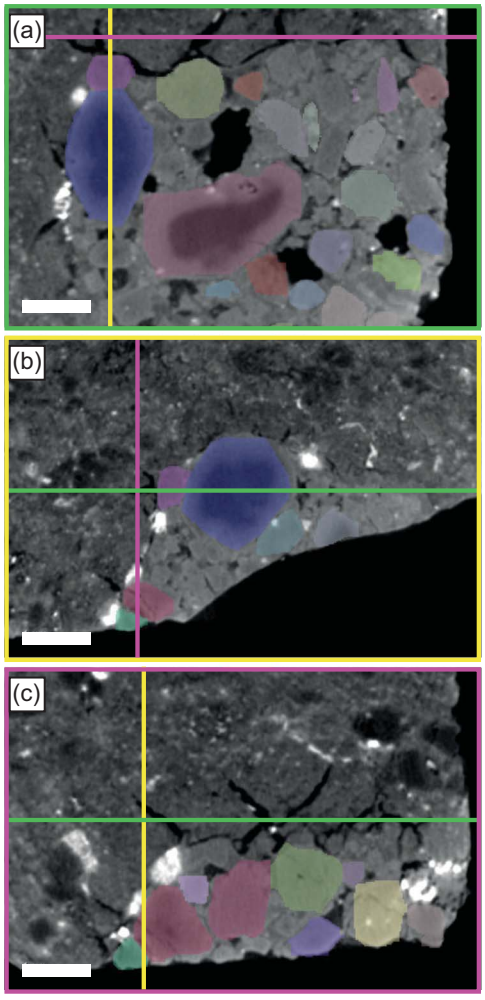

Figure 3. Orthoslices through 3D images illustrating LabDCT-labeled olivine grains overlain on P-ACT data. White bars are 100 µm. Correspondingly colored borders and lines locate each orthoslice within the other two orientations.

morphologies from the P-ACT data to achieve the best possible data quality: high-fidelity grain positions, accurate morphologies, and precise crystallographic information. The individual grain labels (volumes) defined with LabDCT were used as masks from which corresponding 3D data, such as the calibrated P-ACT and/or NM-ACT, can be extracted and later integrated with other measurements and observations. First, using Grainmapper3D, each LabDCT indexed grain was presented according to its own crystallographic axes (i.e., automatically rotating the entire data set such that the orthorhombic axes of a given indexed olivine crystal are presented as the xyz orientations of an image volume). For each grain, the same rotation factors were applied to the corresponding P-ACT data, and 3D bounding boxes were then used to crop to, and so extract, individual grains' LabDCT and P-ACT data for analysis.

Measurements and calculations on an individual grain basis. The qualitative features and calculated measurements were merged to form a database of composition and physical parameters specific to individual grains. Table 2 summarizes the qualitative features that were assessed visually from each of the cropped data sets. Shape factors such as size and aspect ratio were computed using Grainmapper3D. The image data were read using Python as NumPy arrays and used to calculate bulk composition, core composition, zonation intensity, etc., as follows.

Bulk composition calculation is straightforward and involves averaging the composition estimated by each voxel within a grain (after one erosion step to avoid partial volume effects at the crystal edges). In preparation for core-composition calculation, 1D profiles were extracted across the center of the grains (corresponding to the center of the image due to the standardized crystallographic orientation and cropping) in x, y, and z directions and smoothed by a rolling window with a kernel size of 3. A computationally efficient and reproducible method to estimate a core composition for each grain was to average the minimum values of these three smoothed, crystallographically oriented, and grain-centered profiles (see Online Materials[1]). The estimations verified well against the results of several manually located core compositions. This simple approach is valid only because, in our case, normal zonation was universal: more complex zonation styles would require a more sophisticated method of automation to be fully accurate. Furthermore, one grain was removed from the automated compositional zonation assessment due to the presence of a bifurcating crack (a low-density feature through the center of the grain). Using the simple analytical approach, this scenario appears the same as if the grain contained a high Fo core (see Online Materials[1] Fig. S4). Zonation intensity is derived from the difference between maximum and minimum composition values (Fo range) of each grain.

Results

Description of NWA 11346

LabDCT data illustrate the positions, sizes, and crystallographic orientations of 52 olivine grains >100 µm throughout the sample in 3D (Fig. 2). Olivine is clustered in the chondrule as expected, and otherwise is evenly distributed throughout the sample matrix. There is no preferred crystallographic orientation throughout the sample. Other features are revealed in the P-ACT data that have no obvious surface expression, such as a conspicuous, comparatively large, dark region (Online Materials[1] Fig. S2). Importantly, the LabDCT data rule this out as an olivine grain due to the absence of any diffraction spots that can be reconstructed using the crystallography of olivine in that 3D position.

Figure 3 presents orthogonal slices through the ROI with the P-ACT data (grayscale) overlain in color by grains indexed by LabDCT. Grains below the size threshold are not indexed, and in the absence of an overlay, they illustrate the distinct crystal boundaries revealed by the P-ACT imaging. Some minor mismatches in the LabDCT data are observed at the edges of some grains in the P-ACT data, which are observed and explored in detail using other natural samples in Chen et al. (2024). Figures 4a–4c show the positions, morphologies, and crystallographic orientations of the 77 grains >50 µm overlaid with the P-ACT results from the chondrule ROI. There is no preferred crystallographic orientation observed within the ROI.

Integrated 3D observations of grains

We used the database of individual grains to plot integrations of several petrographic parameters. Qualitative textural observations (cracks, inclusions, etc.) do not appear to correspond to composition, size, or form any spatial pattern, see Online Materials[1] Figure S3. Patterns do result, however, when integrating between and across quantitative textural and chemical measurements.

The zonation intensity of each grain is plotted as a function of its rank order in Figure 5. Overlaying core composition and illustrating 3D size strengthens three clear groupings. Those grains that exhibit a range of >25 Fo units are described as strongly zoned (6 grains). These six also have the most primitive cores in the data set, and have a large average grain size, including the largest four grains in the chondrule. The moderately zoned group corresponds to a range between 15 and 25 Fo units (5 grains), with primitive to slightly less primitive cores and an average moderate size. The weakly zoned group is characterized by a range of <15 Fo units (66 grains or ~85% of the population) and typically has more evolved core compositions with a small average size.

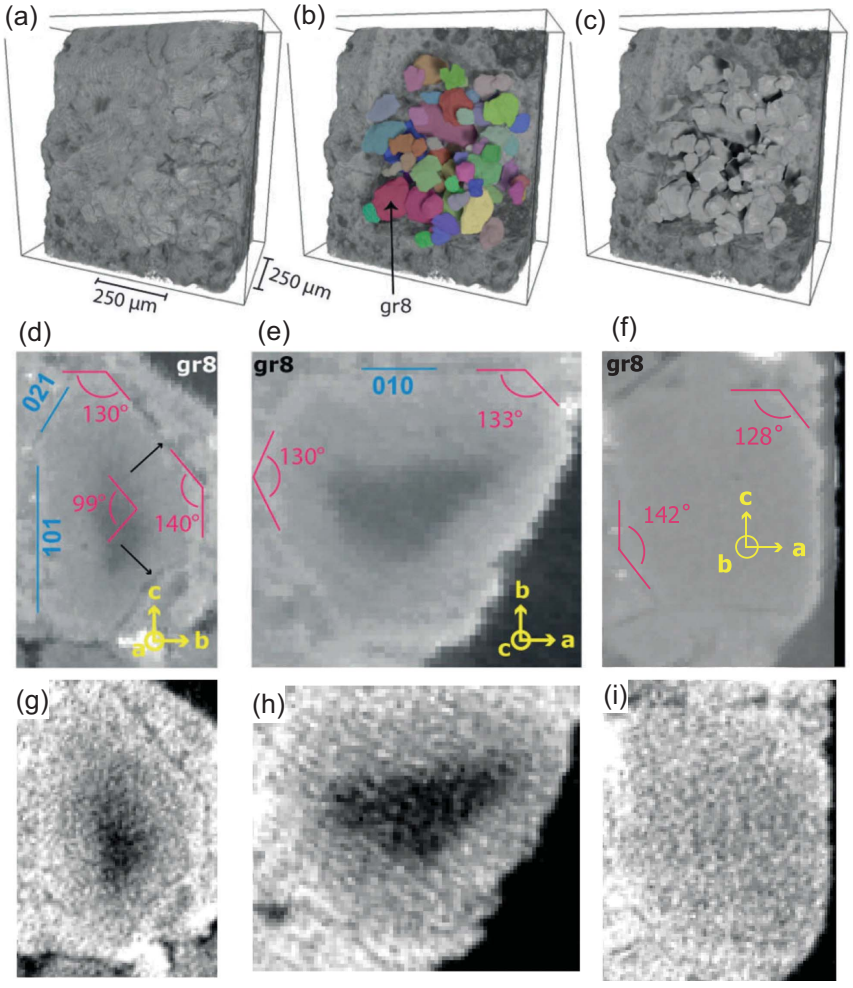

Figure 4. Combined multimodal X-ray imaging results from a chondrule within NWA 11346 (carbonaceous chondrite) highlighting the ability to interrogate individual grains within their own crystallographic context. (**a**) 3D rendering of sample within the ROI (width × height × depth = 0.9 × 0.9 × 0.5 mm) using P-ACT data (see Fig. 2 for location). (**b**) Partial P-ACT data cut-away of (**a**) highlighting the LabDCT reconstruction of olivine grains within a chondrule. Coloration as in Figure 2. (**c**) P-ACT data of olivine grains from (**b**), where the labeled grains are used as a mask. (**d**) Slice through P-ACT data after rotation into the crystallographic orientation of grain 8 (gr8) such that x orientation = b-axis, y = c-axis, and z = a-axis. Interfacial angles measured using image analysis tools match those expected of olivine in this orientation with excellent precision. (**e**) The same grain as in (**d**) where x orientation = a-axis, y = b-axis, and z = c-axis. (**f**) x orientation = a-axis, y = c-axis and z = b-axis. (**g**–**i**) NM-ACT data in the same orientations as (**d**–**f**). Some aberration is due to shallow angle rotations required to align the two data sets, and necessary re-binning of the image data.

Grain shape varies from well-formed and euhedral to considerably rounded and does not correlate to size or composition. In Figure 6, the Feret aspect ratio is plotted against bulk composition (not core composition, as is the case in Fig. 5) and is also colored by bulk composition and again presented by size. Intriguingly, and while there is no clear relationship between aspect ratio and zonation intensity nor with core composition overall, the two most rounded grains in the data set of 77 by a clear margin are both from the group that represents <10% of the grain population: the group of six strongly zoned grains with the most primitive cores. Furthermore, the strongly zoned group can be observed to form a near-linear trend of bulk compositions ranging from Fo_{100} to Fo_{89}, which covary with both grain shape and size; with decreasing bulk Fo, the grains become smaller and rounder.

It is straightforward to assess these grains' spatial locations, resulting in the observation that together they are restricted to a band-like geometry within the chondrule. Furthermore, this visualization shows that the crystallographic orientations of three of the grains are strikingly similar (Fig. 5 inset), and the other three are not dissimilar. Moderately zoned grains are distributed around this band (Fig. 5) and do not show a crystallographic orientation preference. Weakly zoned grains do not show an obvious pattern in either spatial distribution or crystallographic orientation.

Discussion

Observed patterns rely on preserved context

We interpret the trend of six strongly zoned crystals in Figures 5 and 6 as recording the process of Fo_{100} melting during chondrule formation. Their decreasing size with increasing degree of rounding is consistent with grains that have undergone melting from the outside, whereby the dissolution fronts converge at the edges of faces and progressively round off geometric

Table 2. Feature assessment of individual grains (n = 77 within ROI)

	Observed		Not observed
Cracks/voids[a]	12 grains		all other grains
High density inclusions[b,d]	Within core	In margin/at rim	No inclusions observed
	14 grains	7 grains	all other grains
Zonation[c]	Extremely zoned	Moderately zoned	Slight to no zonation
	6 grains	5 grains	all other grains

[a]Each grain was individually observed for cracks and voids, which are identified as regions with the attenuation of air present in either curvilinear or oblate forms in 3D.
[b]High-density inclusions are interpreted from conspicuously bright features >5 voxels in all directions.
[c]Zonation is also quantified (see text and Fig. 5).
[d]We considered bright regions >5 voxels across their minimum axes likely to be high-density inclusions.

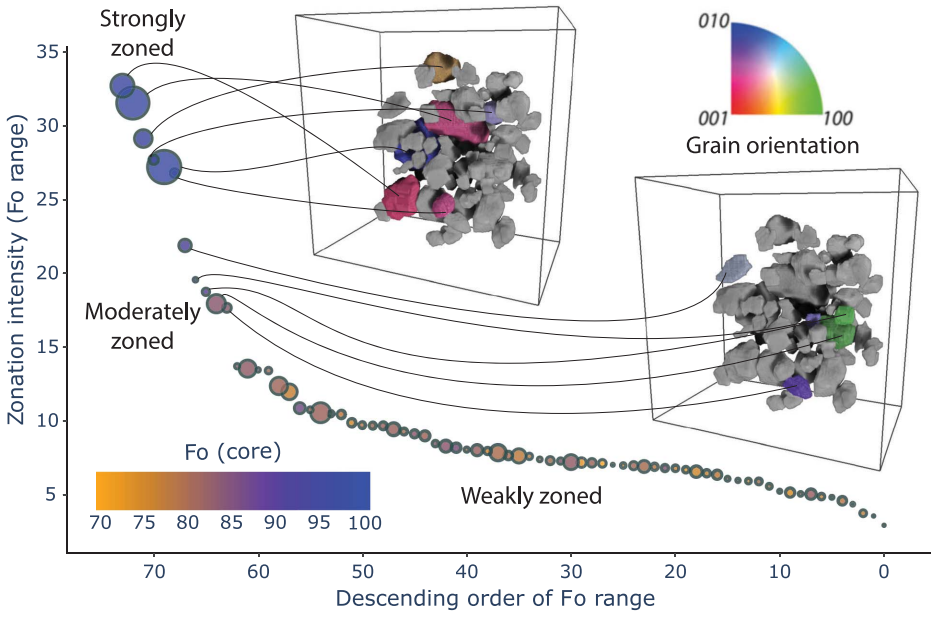

Figure 5. Assessment of zonation intensity derived from 3D crystallographically defined composition profiles of olivine grains and their distribution within a chondrule. Zonation intensity is derived from the difference between maximum and minimum composition values (Fo range) of each grain, which is in turn derived from three crystallographically oriented 1D profiles passing through its center (calibrated P-ACT image intensity). Three natural groupings are evident when arranged in rank order: low zonation intensity <15 Fo units, moderate zonation intensity between 15 and 25 Fo units, and high zonation intensity >25 Fo units in range. Grain size is indicated by relative size of the markers. Insets are ROI from Figure 2 in the same aspect as in Figures 4a–4c. Strongly zoned grains are spatially restricted to a band-like zone in the center of the ROI, whereas moderately zoned grains are located outboard of this band.

shapes. It cannot be known what the original texture and orientation of the precursor was, but it is conceivable that one or more comparatively large grains existed before being mostly melted, and the relict portions remained in more-or-less the same relative orientation before cooling and crystallization. The subsequent overgrowth and diffusion act evenly upon these relict grains, meaning those with initially smaller sizes are more fully overprinted by diffusion, reaching proportionately further into their centers and raising their bulk Fe concentration. At the same time, the composition of the interior of larger relicts persists due to their greater distance from overgrowth boundaries. According to this hypothesis, the two most rounded grains can be considered "reset relicts," and identification of these has implications for testing petrogenetic hypotheses with targeted in situ chemical and isotopic analysis.

The group of weakly zoned crystals likely reflects an origin via nucleation and growth from the chondrule melt, tracking the chondrule's cooling path. The moderately zoned crystal group (marked with open squares in Fig. 6) is more similar to the intensely zoned group in terms of core composition than they are to that of the weakly zoned group. The core composition histogram (Fig. 6) shows that the moderately zoned crystals correspond to an otherwise unpopulated range between the main peak in grain core composition frequency and the (subtle) outlying peak of the intensely zoned group. This observation may indicate the moderately zoned crystals' cores were either also relict (and variably reset by diffusion), or that they nucleated prior to the main onset of nucleation at ~Fo_{80}.

Classic evidence for relict grains, including very high Fo core content and uneven zone boundaries, is clear in the largest crystals, and 2D views can readily identify them as such. However, these features are less convincing with decreasing grain size when viewed in isolation, as they would be by fortuitous sectioning to reveal them. It is only as part of a trend formed by multiple physical and chemical parameters that all six grains can be hypothesized as relicts, and only when strengthened by the spatial and crystallographic relationships observed does the petrogenesis become clear. Indeed, the grains of this trend are outliers according to population-level analysis of core composition (Fig. 6, right-side histogram) and are hidden in the crowd of population-level shape analysis (top histogram), which are both skewed Gaussian distributions. Without their accurate measurement and integration on an individual grain basis, which is impossible to achieve without 3D data, this shape-size-composition-spatial-crystallographic trend would not be detectable. It follows that the non-destructive method of their measurement is the critical factor in gaining this insight.

Combining perspectives to avoid inaccuracies

The 3D volumetric nature of micro-CT data means that the size, shape, surface area, etc., of grains can be measured directly, without out-of-plane uncertainty or stereographic errors. Petrographic observations such as zonation, cracks, inclusions, embayments, etc., can also be made with high confidence, because the presence of such features can be observed in 2D, yet their absence cannot be confirmed in 2D. It is with multimodal X-ray imaging, however, that perspectives can be merged to gain further accuracy.

For instance, one grain in the ROI (Online Materials[1] Fig. S4) exhibits a crack across its middle. Automated mineralogy in 2D

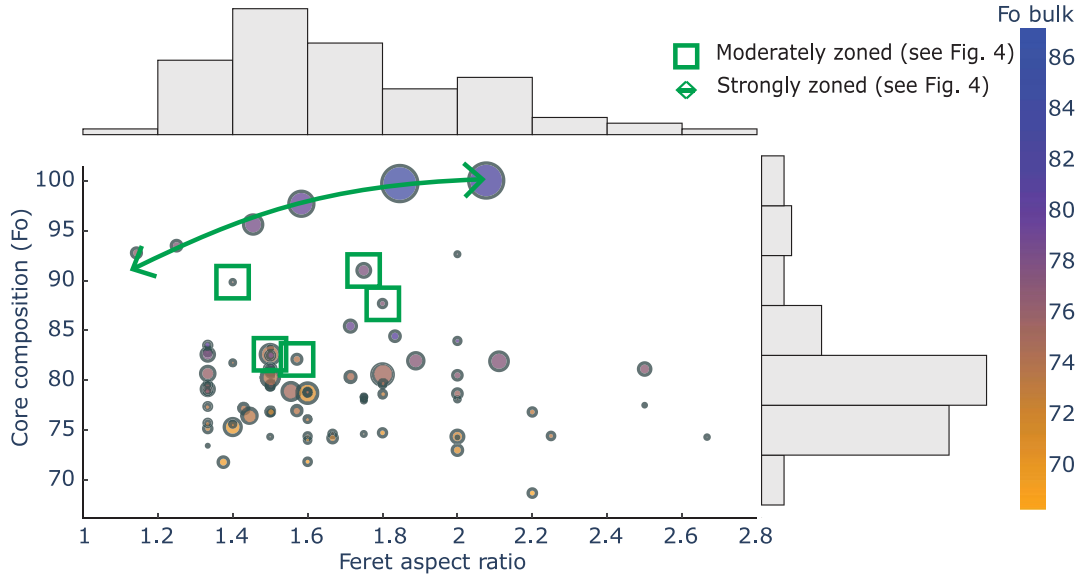

Figure 6. Integrated quantitative 3D measurements of individual olivine grains within a chondrule. Core composition (P-ACT image intensity) plotted against true 3D aspect ratio (Feret max/Feret min) from 76 individual grains (one discarded from automated analysis due to a bisecting crack, see Online Materials[1] Fig. S4). Mean composition of the entire crystal is indicated by color. Relative crystal size is indicated by marker size.

using SEM, or 3D image analysis and phase labeling using ACT, would plausibly count this grain as two distinct grains due to the separation of regions, depending on how sensitive a 3D watershed filter would be applied in the latter case. These common features in rocks can therefore lead to incorrect grain count, size distribution, etc., which may introduce further bias in downstream data reduction, integration, and interpretation. The observations from LabDCT data, however, demonstrate there is no more than a 5° misorientation between each part of the grain. Furthermore, the crystallographically oriented views illustrate that the grain's euhedral shape continues across parts and interfacial angles are close to those expected (Online Materials[1] Fig. S4). The 3D morphological observations provide confidence for petrological reconstruction as one grain, and it is conceivable that by combining proximity and crystallographic analysis, such feature "corrections" may be automatable.

Advancing 3D mineralogy and petrography

A mineral's structure is, by definition, a diagnostic feature along with composition. Interpreting mineralogy by using a proxy for composition only, as with X-ray absorption imaging, meets non-trivial challenges when analyzing samples containing minerals with similar densities, and/or with heterogeneous compositions. It also requires a priori knowledge of the minerals contained within the sample.

This challenge arises because minerals do not have unique densities, and minerals with more than two end-member compositions (such as pyroxenes, feldspars, and garnets, among many other mineral families) have a range of compositions with the same density. These common scenarios result in X-ray absorption contrast images wherein different minerals produce broad peaks in histograms of brightness that overlap significantly, and as such, can be challenging to deconvolve with certainty. Furthermore, textural variation of minerals, such as the presence of micro-inclusions, can significantly modify the apparent density of a region within a crystal by convolution if measured at a resolution coarser than those features. Finally, chemical zoning in single crystals causes extended overlaps between the densities of minerals of different types. Hence, density itself is neither diagnostic nor always reliable. Automated 3D mineralogy using conventional micro-CT alone is therefore fundamentally limited.

Methods have been developed to push this limitation. Machine learning approaches to absorption image analysis with the aim of segmentation are most successful in cases where density and textural differences are both considerable and consistent (Chauhan et al. 2016; Hekler et al. 2019; Gobert et al. 2020). The brightness value of a given voxel, as well as its relationship to its local and non-local neighborhood, are important parameters used for decisions within algorithmic image analysis. The performance of freely available image segmentation tools [e.g., WEKA, a plugin of ImageJ (Arganda-Carreras et al. 2017)] can be highly accurate when the aim is to segment mineral groupings, for example, distinguishing metals from sulfides from silicates. The corollary is that performance lessens when the variation in density and texture between phases that need to be segmented from one another is subtle. Furthermore, the more specific and detailed any training process is (supervised learning), the less accurate the results can be when the same training result is applied to other images. Typically, the assumptions required to assign a voxel to a mineral species are carried through such algorithms and will always support a result, but not always report an uncertainty value. For further reading on the subject of image segmentation, we direct the reader to Andrew (2018), Abdulateef and Salman (2021), and Minaee et al. (2022).

In principle, using LabDCT together with ACT, the mineralogist is enabled to cross-reference structure against density for a given region in a 3D image and avoid the limitations described above. It raises the possibility of considering several plausible

mineralogical assignments to raw data from each approach's first principles, and using the results to converge toward a correct mineral identification.

There are several practical advantages that draw upon combined densitometric and crystallographic measurements. As illustrated by Figures 3 and 4, individual crystals or crystal domains can be digitally oriented and visualized according to their own crystallographic reference frame. This constitutes the basis for advanced characterization and comparisons of crystal morphologies because each crystal can be assessed in an internally consistent manner (underpinning Figs. 4 and 5). For instance, the expression, dimensions, and size ratios of crystal faces in 3D can be used to characterize and interpret grains in ways that would be impossible with 2D data or require significant effort and assumptions (e.g., Barbee et al. 2020). Placing 3D crystal compositions in 3D crystallographic contexts presents opportunities to better constrain growth and diffusion histories. It allows volumetric descriptions of mineral growth and crystal populations genetically linked by, in our case, pre-existing grains, as well as igneous liquid lines of descent. Hence, an improvement from more simplistic chemical populations that do not account for mineral or compositional volume can define a new standard [see George and Gaidies (2017) and Gaidies and George (2021) for studies that integrate crystallographically oriented and volumetrically contextualized compositional data from metamorphic rocks]. All these parameters and their trends can also now be assessed spatially in 3D (see Fig. 5).

Finally, the ability to view 3D maps provides a basis for highly efficient and targeted downstream analysis. The ability to assess where a 2D plane should be cut to maximize the scientific value of in situ analysis provides an advantage. Since sample representation is boosted by observing more rock volume, it could be argued that the underlying reason for making a random slice (representation) is superseded by the advent of 3D mineralogical data. Now, investigators may find a targeted 2D slice, such as the one that intersects more crystals of a certain type (e.g., the relict grains for contextualized isotopic measurements or untangling the questions of the moderately zoned grains using trace element observations), or one that exposes a rare feature (e.g., the chondrule or unknown low-density phase, see Online Materials[1] Fig. S2). In these cases, the 2D slice would be deliberately unrepresentative, yet it does not generate a source of unquantified bias because having 3D data means representation and context are already established and will always be retained.

Accessing all perspectives, all at once

Figures 4d–4f highlight the ability of multi-modal X-ray imaging to observe a choice of 2D cross sections of any grain within its own 3D crystallographic reference frame. The high angular precision of LabDCT is demonstrated by our chosen cross sections that exhibit interfacial angles matching those expected for olivine's crystal forms (Welsch et al. 2013; Pankhurst et al. 2019). This ability was pursued in support of the automated assessment of zonation intensity described above, but also had another result.

We find the agreement between expected and observed interfacial angles to be noteworthy for two reasons. First, all the grains can be morphologically assessed without assumptions about how ideal they are, meaning observed deviation from an ideal form can provide insight. Absorption contrast imaging can be used to conduct shape analysis and derive crystallography, but it is not without assumptions. Second, direct 3D observation can remove the perception of a lack of crystal symmetry simply because 2D observations rarely reveal ideal crystal forms due to random sectioning angles. At least for our case, symmetry is the rule, but without a method of presenting each grain according to its crystallographic axes, it appeared to be the exception.

The modern need for 3D mineralogy and petrography

How minerals are classified is a paradigm that has recently attracted new thinking and debate (Hazen 2019, 2021; Hatert et al. 2021). Chemistry and structure are universally regarded as essential pillars upon which mineral species can be distinguished, and represent a convention held by mineralogists for generations (Dana 1837). Crystal form, habit, mineral associations and natural kinds, and temporal considerations have also been suggested to be important factors in highlighting meaning and significance; hence, these are proposed to also hold value in classification schema (Hazen et al. 2022). Yet while structure and composition can be determined by conventional techniques, determining form and associations cannot be unequivocally achieved using 2D observations as outlined above. The drive to characterize and classify minerals using expanded, rich, and more meaningful schema adds to our motivation to develop 3D petrographic techniques that have obvious potential to support such work.

Applied mineralogical study is fundamental to mining, metallurgy, geoengineering, and environmental management (e.g., Kerisit et al. 2013; Rigopoulos et al. 2015; Dominy et al. 2018; Lishchuk et al. 2020). Improvements in mineralogical observation and data processing have led to discoveries and operational advantages (e.g., Sutherland and Gottlieb 1991; Van Rythoven et al. 2021). One focus for development has been to increase the speed and degree of analysis automation, leading to a range of branded "automated mineralogy" technologies that have been applied across geoscience (e.g., Pirrie et al. 2004; Leißner et al. 2016; Hornby et al. 2019; Schulz et al. 2019; Pankhurst et al. 2022; Liu et al. 2022). The macroeconomic shift currently underway from fossil fuels to renewable energies relies on the increased use of raw materials and thus mining (e.g., Haque et al. 2014), which has increasingly become a policy priority (e.g., Hammond and Brady 2022; Cervantes Barron et al. 2023). A concomitant change in public perception and government policy toward sustainable practices and the importance of mineralogy to, for example, precious metal and rare earth element mining (e.g., Liu et al. 2022), supports a view that the quality of mineralogical knowledge and innovative applications will only grow in importance.

Implications

The application of LabDCT together with quantitative absorption contrast imaging marks a milestone in accessibility for 3D petrography. There is now another option emerging for gathering in situ crystallographic data: with laboratory scanners, rather than at brilliant light sources. Publications and

abstracts to date have progressed from olivine (Pankhurst et al. 2019; Boneh et al. 2021; Shea et al. 2021) to chromite (Chen et al. 2023, 2024) quartz (Barbee et al. 2024), and ice (Barbee et al. 2025), but diffraction contrast imaging will require extensive development and testing before it can mature to widespread applicability and deliver greater value to petrography.

By way of comparison, micro-CT is routine in various industries, including oil and gas, many materials and life sciences, and medicine. Its application as a research tool has increased in geoscience, where smaller communities, such as paleontology and volcanology, are delivering innovations. However, to date, it has rarely been regarded as essential infrastructure in geoscience departments and geological surveys (Mees et al. 2003; Cnudde and Boone 2013).

If the trajectory of LabDCT follows that of absorption X-ray imaging, it will plausibly be >10 years before the technique could be considered a fundamental imaging modality used routinely by geoscientists. However, this study implies that a multimodal X-ray imaging system is greater than the sum of its parts. Neither modality alone would be able to derive meaning from these grains in the integrated way we have demonstrated. This greater potential insight supports a view that multimodal X-ray tomography will cut a more direct path to users. Finally, its non-destructive nature places it as a first-step technology for downstream sample preparation and analysis, from which data can be placed back into the 3D "digital copy." These correlative workflows are becoming increasingly popular as their value is demonstrated (e.g., Warlo et al. 2021), and each analytical technology is considered not only for the data they generate but also how their data complement those gained from others.

Acknowledgments and Funding

This work was carried out with the support of the Diamond Light Source and Diamond Manchester Collaboration beamtime award 19526. Data were acquired during beamtime MT19526-1 "Densitometry: a fundamental study of electron density mapping and calibration," Rhian Jones, 2018. This research used a resource of the National Synchrotron Light Source II, a U.S. Department of Energy (DOE) Office of Science User Facility operated for the DOE Office of Science by Brookhaven National Laboratory under Contract No. DE-SC0012704. The authors thank Kaz Wanelik for their help in beamtime preparation and Lewis Hughes (University of Manchester) for assistance with SEM analysis. Dobson was supported by NE/M018687/2. T. Müller is thanked for his editorial handling and suggestions, which improved the manuscript. Two anonymous reviewers are thanked for their constructive criticisms which also improved the manuscript.

References Cited

Abdulateef, S. and Salman, M. (2021) A Comprehensive Review of Image Segmentation Techniques. IJEEE, 17(2), 166–175, doi:10.37917/ijeee.17.2.18.

Andrew, M. (2018) A quantified study of segmentation techniques on synthetic geological XRM and FIB-SEM images. Computational Geosciences, 22(6), 1503–1512, doi:10.1007/s10596-018-9768-y.

Arganda-Carreras, I., Kaynig, V., Rueden, C., Eliceiri, K.W., Schindelin, J., Cardona, A., and Sebastian Seung, H. (2017) Trainable Weka Segmentation: A machine learning tool for microscopy pixel classification. Bioinformatics (Oxford, England), 33, 2424–2426, https://doi.org/10.1093/bioinformatics/btx180.

Bachmann, F., Bale, H., Gueninchault, N., Holzner, C., and Lauridsen, E.M. (2019) 3D grain reconstruction from laboratory diffraction contrast tomography. Journal of Applied Crystallography, 52(3), 643–651, doi:10.1107/S1600576719005442.

Barbee, O., Chesner, C., and Deering, C. (2020) Quartz crystals in Toba rhyolites show textures symptomatic of rapid crystallization. American Mineralogist, 105, 194–226.

Barbee, O.A., Pankhurst, M.J., Bachmann, F., Oddershede, J., and Sun, J. (2024) A sinusoidal twin boundary harmonizes with the elastic anisotropy of quartz. PREPRINT (Version 1) available at Research Square, https://doi.org/10.21203/rs.3.rs-3949818/v1.

Barbee, O., Oddershede, J., Purohit, R.P., Ånes, H., Engqvist, J., Svensson, A., Rathmann, N., Blunier, T., Bachmann, F., and Hall, S. (2025) Mapping textures of polar ice cores using 3D laboratory X-ray microscopy. EarthArXiv preprint, https://doi.org/10.31223/X52Q89.

Boneh, Y., Chin, E.J., Chilson-Parks, B.H., Saal, A.E., Hauri, E.H., Hearn, C. Jr., and Hirth, G. (2021) Microstructural shift due to post-deformation annealing in the upper mantle. Geochemistry, Geophysics, Geosystems, 22(3), e2020GC009377, doi:10.1029/2020GC009377.

Brearley, A.J. and Jones, R.H. (1998) Chondritic meteorites. Reviews in Mineralogy and Geochemistry, 36, 3-01–3-398.

Carlson, W.D. and Denison, C. (1992) Mechanisms of porphyroblast crystallization: Results from high-resolution computed X-ray tomography. Science, 257(5074), 1236–1239, doi:10.1126/science.257.5074.1236.

Cashman, K.V. (2020) Crystal size distribution (CSD) analysis of volcanic samples: Advances and challenges. Frontiers in Earth Science (Lausanne), 8, 291, doi:10.3389/feart.2020.00291.

Cervantes Barron, K., Dhir, S., and Cullen, J.M. (2023) The geopolitics of critical materials and minerals and implications for the low-carbon transition. University of Cambridge, Climate Compatible Growth, p. 1–14.

Chauhan, S., Rühaak, W., Anbergen, H., Kabdenov, A., Freise, M., Wille, T., and Sass, I. (2016) Phase segmentation of X-ray computer tomography rock images using machine learning techniques: An accuracy and performance study. Solid Earth, 7(4), 1125–1139, doi:10.5194/se-7-1125-2016.

Chen, X., Godel, B., and Verrall, M. (2023) Comparison of laboratory diffraction contrast tomography and electron backscatter diffraction results: Application to naturally occurring chromites. Microscopy and Microanalysis, 29(6), 1901–1920, doi:10.1093/micmic/ozad130.

——— (2024) Postprocessing Workflow for laboratory diffraction contrast tomography: A case study on chromite geomaterials. Microscopy and Microanalysis, 30(3), 440–455, doi:10.1093/mam/ozae036.

Cnudde, V. and Boone, M.N. (2013) High-resolution X-ray computed tomography in geosciences: A review of the current technology and applications. Earth-Science Reviews, 123, 1–17, doi:10.1016/j.earscirev.2013.04.003.

Couperthwaite, F.K., Morgan, D.J., Pankhurst, M.J., Lee, P.D., and Day, J.M.D. (2021) Reducing epistemic and model uncertainty in ionic inter-diffusion chronology: A 3D observation and dynamic modeling approach using olivine from Piton de la Fournaise, La Réunion. American Mineralogist, 106(3), 481–494, doi:10.2138/am-2021-7296CCBY.

Dana, J.D. (1837) The System of Mineralogy, 1333 p. Wiley.

Deer, W.A., Howie, R.A., and Zussman, J. (1992) An Introduction to the Rock-Forming Minerals, 696 p. Longman.

Dominy, S.C., O'Connor, L., Parbhakar-Fox, A., Glass, H.J., and Purevgerel, S. (2018) Geometallurgy—A route to more resilient mine operations. Minerals, 8(12), 560, doi:10.3390/min8120560.

Fernandez, R. and Moisy, C. (2021) Fijiyama: A registration tool for 3D multimodal time-lapse imaging. Bioinformatics (Oxford, England), 37, 1482–1484, https://doi.org/10.1093/bioinformatics/btaa846.

Fitton, J.G. and Godard, M. (2004) Origin and evolution of magmas on the Ontong Java Plateau. Special Publication – Geological Society of London, 229, 151–178, https://doi.org/10.1144/GSL.SP.2004.229.01.10.

Fleet, M.E. (1978) Origin of olivine subgrain boundaries in mantle peridotites. Nature, 275(5675), 48–50, doi:10.1038/275048a0.

Foley, S.F., Venturelli, G., Green, D.H., and Toscani, L. (1987) The ultrapotassic rocks: Characteristics, classification, and constraints for petrogenetic models. Earth-Science Reviews, 24(2), 81–134, doi:10.1016/0012-8252(87)90001-8.

Gaidies, F. and George, F.R. (2021) The interfacial energy penalty to crystal growth close to equilibrium. Geology, 49(8), 988–992, doi:10.1130/G48715.1.

Gattacceca, J., Bouvier, A., Grossman, J., Metzler, K., and Uehara, M. (2019) The Meteoritical Bulletin, No. 106. Meteoritics & Planetary Science, 54(2), 469–471, doi:10.1111/maps.13215.

George, F.R. and Gaidies, F. (2017) Characterisation of a garnet population from the Sikkim Himalaya: Insights into the rates and mechanisms of porphyroblast crystallisation. Contributions to Mineralogy and Petrology, 172(7), 57, doi:10.1007/s00410-017-1372-y.

Gobert, C., Kudzal, A., Sietins, J., Mock, C., Sun, J., and McWilliams, B. (2020) Porosity segmentation in X-ray computed tomography scans of metal additively manufactured specimens with machine learning. Additive Manufacturing, 36, 101460, doi:10.1016/j.addma.2020.101460.

Hammond, D.R. and Brady, T.F. (2022) Critical minerals for green energy transition: A United States perspective. International Journal of Mining, Reclamation and Environment, 36(9), 624–641, doi:10.1080/17480930.2022.2124788.

Hanna, R.D. and Ketcham, R.A. (2017) X-ray computed tomography of planetary materials: A primer and review of recent studies. Chemie der Erde, 77(4), 547–572, doi:10.1016/j.chemer.2017.01.006.

Hansen, L.N., Zimmerman, M.E., and Kohlstedt, D.L. (2012) The influence of microstructure on deformation of olivine in the grain-boundary sliding regime. Journal of Geophysical Research: Solid Earth, 117, 2012JB009305, doi:10.1029/2012JB009305.

Haque, N., Hughes, A., Lim, S., and Vernon, C. (2014) Rare earth elements: Overview of mining, mineralogy, uses, sustainability and environmental impact. Resources, 3(4), 614–635, doi:10.3390/resources3040614.

Hatert, F., Mills, S.J., Hawthorne, F.C., and Rumsey, M.S. (2021) A comment on "An evolutionary system of mineralogy: Proposal for a classification of planetary materials based on natural kind clustering." American Mineralogist, 106(1), 150–153, doi:10.2138/am-2021-7590.

Hazen, R.M. (2019) An evolutionary system of mineralogy: Proposal for a classification of planetary materials based on natural kind clustering. American Mineralogist, 104(6), 810–816, doi:10.2138/am-2019-6709CCBYNCND.

——— (2021) Reply to "A comment on 'An evolutionary system of mineralogy: Proposal for a classification of planetary materials based on natural kind clustering.'" American Mineralogist, 106(1), 154–156, doi:10.2138/am-2021-7773.

Hazen, R.M., Morrison, S.M., Krivovichev, S.V., and Downs, R.T. (2022) Lumping and splitting: Toward a classification of mineral natural kinds. American Mineralogist, 107(7), 1288–1301, doi:10.2138/am-2022-8105.

Hekler, A., Utikal, J.S., Enk, A.H., Solass, W., Schmitt, M., Klode, J., Schadendorf, D., Sondermann, W., Franklin, C., Bestvater, F., and others. (2019) Deep learning outperformed 11 pathologists in the classification of histopathological melanoma images. European Journal of Cancer, 118, 91–96, doi:10.1016/j.ejca.2019.06.012.

Helz, R.T. (1987) Diverse olivine types in lava of the 1959 eruption of Kilauea volcano and their bearing on eruption dynamics. U.S. Geological Survey Professional Paper, 1350, 691–722.

Holzner, C., Lavery, L., Bale, H., Merkle, A., McDonald, S., Withers, P., Zhang, Y., Jensen, D.J., Kimura, M., Lyckegaard, A., and others. (2016) Diffraction contrast tomography in the laboratory – Applications and future directions. Microscopy Today, 24(4), 34–43, doi:10.1017/S1551929516000584.

Hornby, A.J., Lavallée, Y., Kendrick, J.E., Rollinson, G., Butcher, A.R., Clesham, S., Kueppers, U., Cimarelli, C., and Chigna, G. (2019) Phase partitioning during fragmentation revealed by QEMSCAN Particle Mineralogical Analysis of volcanic ash. Scientific Reports, 9(1), 126, doi:10.1038/s41598-018-36857-4.

Jerram, D.A. and Higgins, M.D. (2007) 3D analysis of rock textures: Quantifying igneous microstructures. Elements, 3(4), 239–245, doi:10.2113/gselements.3.4.239.

Jerram, D.A., Mock, A., Davis, G.R., Field, M., and Brown, R.J. (2009) 3D crystal size distributions: A case study on quantifying olivine populations in kimberlites. Lithos, 112 (Supplement 1), 223–235, doi:10.1016/j.lithos.2009.05.042.

Jones, K.W. (1999) Application of synchrotron radiation in the geological and environmental sciences. Brookhaven National Lab, BNL-66820, https://www.osti.gov/servlets/purl/770806-0YkpGM/webviewable/.

Jones, R.H. (2012) Petrographic constraints on the diversity of chondrule reservoirs in the protoplanetary disk. Meteoritics & Planetary Science, 47(7), 1176–1190, doi:10.1111/j.1945-5100.2011.01327.x.

Jones, R.H., Villeneuve, J., and Libourel, G. (2017) Thermal histories of chondrules: Petrologic observations and experimental constraints. Chondrules and the Protoplanetary Disk, 1963, 2029.

Kahl, M., Chakraborty, S., Costa, F., and Pompilio, M. (2011) Dynamic plumbing system beneath volcanoes revealed by kinetic modeling, and the connection to monitoring data: An example from Mt. Etna. Earth and Planetary Science Letters, 308(1-2), 11–22, doi:10.1016/j.epsl.2011.05.008.

Kerisit, S., Bylaska, E.J., and Felmy, A.R. (2013) Water and carbon dioxide adsorption at olivine surfaces. Chemical Geology, 359, 81–89, doi:10.1016/j.chemgeo.2013.10.004.

Kin, I., Sio, C., and Dauphas, N. (2017) Thermal and crystallization histories of magmatic bodies by Monte Carlo inversion of Mg-Fe isotopic profiles in olivine. Geology, 45(1), 67–70, doi:10.1130/G38056.1.

King, A.J., Mason, E., Bates, H.C., Schofield, P.F., Donaldson Hanna, K.L., Bowles, N.E., and Russell, S.S. (2021) Tracing the earliest stages of hydrothermal alteration on the CM chondrite parent body. Meteoritics & Planetary Science, 56, 1708–1728, https://doi.org/10.1111/maps.13734.

Kuebler, K.E., McSween, H.Y. Jr., Carlson, W.D., and Hirsch, D. (1999) Sizes and masses of chondrules and metal-troilite grains in ordinary chondrites: Possible implications for nebular sorting. Icarus, 141(1), 96–106, doi:10.1006/icar.1999.6161.

Leißner, T., Hoang, D.H., Rudolph, M., Heinig, T., Bachmann, K., Gutzmer, J., Schubert, H., and Peuker, U.A. (2016) A mineral liberation study of grain boundary fracture based on measurements of the surface exposure after milling. International Journal of Mineral Processing, 156, 3–13, doi:10.1016/j.minpro.2016.08.014.

Lishchuk, V., Koch, P.-H., Ghorbani, Y., and Butcher, A.R. (2020) Towards integrated geometallurgical approach: Critical review of current practices and future trends. Minerals Engineering, 145, 106072, doi:10.1016/j.mineng.2019.106072.

Liu, T., Song, W., Kynicky, J., Yang, J., Chen, Q., and Tang, H. (2022) Automated quantitative characterization REE ore mineralogy from the Giant Bayan Obo Deposit, Inner Mongolia, China. Minerals, 12(4), 426, doi:10.3390/min12040426.

Lubbers, J., Kent, A., Meisenheimer, D., and Wildenschild, D. (2023) 3D zoning of barium in alkali feldspar. American Mineralogist, 108(2), 297–311, doi:10.2138/am-2022-8139.

Marsh, B.D. (1998) On the interpretation of crystal size distributions in magmatic systems. Journal of Petrology, 39(4), 553–599, doi:10.1093/petroj/39.4.553.

McDonald, S.A., Reischig, P., Holzner, C., Lauridsen, E.M., Withers, P.J., Merkle, A.P., and Feser, M. (2015) Non-destructive mapping of grain orientations in 3D by laboratory X-ray microscopy. Scientific Reports, 5(1), 14665. doi:10.1038/srep14665.

Mees, F., Swennen, R., Geet, M.V., and Jacobs, P. (2003) Applications of X-ray computed tomography in the geosciences. Geological Society of London, Special Publications, 215(1), 1–6, doi:10.1144/GSL.SP.2003.215.01.01.

Minaee, S., Boykov, Y., Porikli, F., Plaza, A., Kehtarnavaz, N., and Terzopoulos, D. (2022) Image segmentation using deep learning: A survey. IEEE Transactions on Pattern Analysis and Machine Intelligence, 44, 3523–3542, https://doi.org/10.1109/TPAMI.2021.3059968.

Mock, A. and Jerram, D.A. (2005) Crystal size distributions (CSD) in three dimensions: Insights from the 3D reconstruction of a highly porphyritic rhyolite. Journal of Petrology, 46(8), 1525–1541, doi:10.1093/petrology/egi024.

Morgan, D.J. and Jerram, D.A. (2006) On estimating crystal shape for crystal size distribution analysis. Journal of Volcanology and Geothermal Research, 154(1-2), 1–7, doi:10.1016/j.jvolgeores.2005.09.016.

Mourey, A.J. and Shea, T. (2019) Forming olivine phenocrysts in basalt: A 3D Characterization of growth rates in laboratory experiments. Frontiers in Earth Science (Lausanne), 7, 300, doi:10.3389/feart.2019.00300.

Oddershede, J., Bachmann, F., Sun, J., and Lauridsen, E. (2022) Advanced acquisition strategies for lab-based diffraction contrast tomography. Integrating Materials and Manufacturing Innovation, 11(1), 1–12, doi:10.1007/s40192-021-00249-w.

Ostorero, L., Balcone-Boissard, H., Boudon, G., Shapiro, N.M., Belousov, A., Belousova, M., Auer, A., Senyukov, S.L., and Droznina, S.Y. (2022) Correlated petrology and seismicity indicate rapid magma accumulation prior to eruption of Kizimen volcano, Kamchatka. Communications Earth & Environment, 3(1), 290, doi:10.1038/s43247-022-00622-3.

Pankhurst, M.J., Dobson, K.J., Morgan, D.J., Loughlin, S.C., Thordarson, T., Lee, P.D., and Courtois, L. (2014) Directly monitoring the magmas fuelling volcanic eruptions in near-real-time using X-ray micro-computed tomography. Journal of Petrology, 55(3), 671–684, doi:10.1093/petrology/egt079.

Pankhurst, M.J., Walshaw, R., and Morgan, D.J. (2017) Major element chemical heterogeneity in Geo2 olivine microbeam reference material: A spatial approach to quantifying heterogeneity in primary reference materials. Geostandards and Geoanalytical Research, 41(1), 85–91, doi:10.1111/ggr.12134.

Pankhurst, M.J., Fowler, R., Courtois, L., Nonni, S., Zuddas, F., Atwood, R.C., Davis, G.R., and Lee, P.D. (2018a) Enabling three-dimensional densitometric measurements using laboratory source X-ray micro-computed tomography. SoftwareX, 7, 115–121, doi:10.1016/j.softx.2018.03.004.

Pankhurst, M.J., Morgan, D.J., Thordarson, T., and Loughlin, S.C. (2018b) Magmatic crystal records in time, space, and process, causatively linked with volcanic unrest. Earth and Planetary Science Letters, 493, 231–241, doi:10.1016/j.epsl.2018.04.025.

Pankhurst, M.J., Vo, N.T., Butcher, A.R., Long, H., Wang, H., Nonni, S., Harvey, J., Gu finnsson, G., Fowler, R., Atwood, R., and others. (2018c) Quantitative measurement of olivine composition in three dimensions using helical scan X-ray micro tomography. American Mineralogist, 103(11), 1800–1811, doi:10.2138/am-2018-6419.

Pankhurst, M.J., Gueninchault, N., Andrew, M., and Hill, E. (2019) Non-destructive three-dimensional crystallographic orientation analysis of olivine using Laboratory Diffraction Contrast Tomography. Mineralogical Magazine, 83(5), 705–711, doi:10.1180/mgm.2019.51.

Pankhurst, M.J., Scarrow, J.H., Barbee, O.A., Hickey, J., Coldwell, B.C., Rollinson, G.K., Rodríguez-Losada, J.A., Martín Lorenzo, A., Rodríguez, F., Hernández, W., and others. (2022) Rapid response petrology for the opening eruptive phase of the 2021 Cumbre Vieja eruption, La Palma, Canary Islands. Volcanica, 5(1), 1–10, doi:10.30909/vol.05.01.0110.

Philpotts, A.R., Brustman, C.M., Shi, J., Carlson, W.D., and Denison, C. (1999) Plagioclase-chain networks in slowly cooled basaltic magma. American Mineralogist, 84(11-12), 1819–1829, doi:10.2138/am-1999-11-1209.

Pirrie, D., Butcher, A.R., Power, M.R., and others. (2004) Rapid quantitative mineral and phase analysis using automated scanning electron microscopy (QemSCAN); potential applications in forensic geoscience. In K. Pye and D.J. Croft, Eds., Forensic Geoscience: Principles, Techniques and Applications, Vol. 232. Geological Society of London.

Ramachandran, G.N. and Lakshminarayanan, A.V. (1971) Three-dimensional reconstruction from radiographs and electron micrographs: Application of convolutions instead of Fourier transforms. Proceedings of the National Academy of Sciences of the United States of America, 68(9), 2236–2240, doi:10.1073/pnas.68.9.2236.

Rigopoulos, I., Petallidou, K.C., Vasiliades, M.A., Delimitis, A., Ioannou, I., Efstathiou, A.M., and Kyratsi, T. (2015) Carbon dioxide storage in olivine basalts: Effect of ball milling process. Powder Technology, 273, 220–229, doi:10.1016/j.powtec.2014.12.046.

Rose, T.R., Sorensen, S.S., and Post, J.E. (2009) The impurities in the Rockport fayalite microbeam standard: How bad are they? AGU Fall Meeting Abstracts.

Schindelin, J., Arganda-Carreras, I., Frise, E., Kaynig, V., Longair, M., Pietzsch, T., Preibisch, S., Rueden, C., Saalfeld, S., Schmid, B., and others. (2012) Fiji: An open-source platform for biological-image analysis. Nature Methods, 9(7), 676–682, doi:10.1038/nmeth.2019.

Schulz, B., Merker, G., and Gutzmer, J. (2019) Automated SEM mineral liberation analysis (MLA) with generically labelled EDX spectra in the mineral processing of rare earth element ores. Minerals, 9(9), 527, doi:10.3390/min9090527.

Shea, T., Lubbers, J., Mourey, A., et al (2021) Crystallographic orientation of crystal clusters in 3D using laboratory diffraction contrast tomography: initial tests on Kilauea olivine. AGU Fall Meeting Abstracts, V11B–08.

Sutherland, D.N. and Gottlieb, P. (1991) Application of automated quantitative mineralogy in mineral processing. Minerals Engineering, 4(7-11), 753–762, doi:10.1016/0892-6875(91)90063-2.

Taylor, L.A., Keller, R.A., Snyder, G.A., Wang, W., Carlson, W.D., Hauri, E.H., McCandless, T., Kim, K.-R., Sobolev, N.V., and Bezborodov, S.M. (2000) Diamonds and their mineral inclusions, and what they tell us: A detailed "pull-apart" of a diamondiferous eclogite. International Geology Review, 42(11), 959–983, doi:10.1080/00206810009465120.

Uesugi, M., Uesugi, K., and Oka, M. (2010) Non-destructive observation of meteorite chips using quantitative analysis of optimized X-ray micro-computed tomography. Earth and Planetary Science Letters, 299(3-4), 359–367, doi:10.1016/j.epsl.2010.09.016.

Van Rythoven, A., Clark, J., Ray, J., and Felsman, J. (2021) Normative indexes calibrated by automated mineralogy to model a rare earth deposit. Ore Geology Reviews, 139, 104540, doi:10.1016/j.oregeorev.2021.104540.

Vo, N.T., Drakopoulos, M., Atwood, R.C., and Reinhard, C. (2014) Reliable method for calculating the center of rotation in parallel-beam tomography. Optics Express, 22(16), 19078–19086, doi:10.1364/OE.22.019078.

Vo, N.T., Atwood, R.C., and Drakopoulos, M. (2015) Radial lens distortion correction with sub-pixel accuracy for X-ray micro-tomography. Optics Express, 23(25), 32859–32868, doi:10.1364/OE.23.032859.

——— (2018) Superior techniques for eliminating ring artifacts in X-ray micro-tomography. Optics Express, 26(22), 28396–28412, doi:10.1364/OE.26.028396.

Vo, N.T., Atwood, R.C., Drakopoulos, M., and Connolley, T. (2021) Data processing methods and data acquisition for samples larger than the field of view in parallel-beam tomography. Optics Express, 29(12), 17849–17874, doi:10.1364/OE.418448.

Warlo, M., Bark, G., Wanhainen, C., and others. (2021) Multi-scale X-ray computed tomography analysis to aid automated mineralogy in ore geology research. Frontiers of Earth Science, 9, 789372. doi:10.3389/feart.2021.789372.

Welsch, B., Faure, F., Famin, V., Baronnet, A., and Bachèlery, P. (2013) Dendritic crystallization: A single process for all the textures of olivine in basalts? Journal of Petrology, 54(3), 539–574, doi:10.1093/petrology/egs077.

Manuscript received October 2, 2023
Manuscript accepted April 5, 2025
Accepted manuscript online April 30, 2025
Manuscript Handled by Thomas Mueller

Endnotes:

[1]Deposit item AM-25-129213. Online Materials are free to all readers. Go online, via the table of contents or article view, and find the tab or link for supplemental materials.